AIAA JOURNAL
Vol. 33, No. 8, August 1995

Numerical Simulation of Oblique Shock-Wave/Vortex Interaction

Donald P. Rizzetta*
U.S. Air Force Wright Laboratory, Wright–Patterson Air Force Base, Ohio 45433-7913

High Reynolds number supersonic flowfields were generated numerically by integration of the time-dependent three-dimensional compressible Euler and mass-averaged Navier–Stokes equations in order to simulate the interaction of a streamwise vortex with an oblique shock wave. The vortex develops at the tip of a vortex-generating fin which is suspended from the ceiling of a wind tunnel. Downstream, an oblique shock wave is produced by a wing surface which spans the width of the wind tunnel and has a two-dimensional sharp leading-edge wedge as its airfoil section. Grid resolution studies are provided in order to assess accuracy of the solutions. Resultant features of the numerical flowfields are discussed, and comparison is made with experimental data in terms of static pressure distributions on the wing surface.

Nomenclature

C_p	= static pressure coefficient
c	= airfoil reference chord
d	= streamwise distance from vortex generator to wing leading edge
h	= vertical height of vortex generator above wing leading edge
$\overline{N^+}$	= average number of grid points for which $y^+ < 10$
x, y, z	= nondimensional Cartesian coordinates in streamwise, spanwise, and vertical directions
y^+	= law-of-the-wall coordinate
$\overline{y^+}$	= average value of y^+ at first mesh point away from surface
α	= vortex generator angle of attack
$\Delta S_\xi, \Delta S_\eta, \Delta S_\zeta$	= mesh spacing in ξ, η, ζ directions
ξ, η, ζ	= computational coordinates

Subscript

le	= evaluated at wing leading edge

Introduction

THE interaction between a streamwise vortex intersecting an oblique shock wave produces a complex three-dimensional flowfield that can occur in a number of both internal and external flows. Such situations commonly involve vortices that may be produced by the forebodies and lifting surfaces of supersonic vehicles or from the tips of canards, fins, and wings. These vortices then respond to the associated shock systems present over wings or control surfaces or within high-speed inlets. In the case of rotorcraft operating at supercritical Mach numbers, the shock waves formed on blade surfaces interact with trailing tip vortices, in the wake of preceding blades, to generate the acoustic phenomenon known as blade slap.[1] Similarly, "shock associated jet noise" is produced in the plume of a jet engine operating at supercritical pressure ratios when turbulent eddies in the jet impinge upon the trailing shock-wave system.[2] This broadband noise is an important design factor because of its impact on the surrounding environment, as well as its effect on structural fatigue.

Shock-wave/vortex interactions are, in general, three dimensional and unsteady. They may result in a loss of lift, an increase in drag, and rapid variations in pitching moment that can adversely affect aerodynamic performance, as well as stability and control characteristics. When such occurrences are sufficiently strong, vortex breakdown may be present.

Because of the interesting physical nature and practical implications of shock-wave/vortex interactions, a number of experimental and numerical investigations have been conducted in order to understand their basic features.[3–13] Many of the experimental studies have considered vortical impingement on normal shock waves.[3,4,6,11] Because of the strength of the resulting interactions, such flows were often characterized by vortex breakdown and unsteadiness. The investigations of Kalkhoran et al.,[9] Kalkhoran,[12] and Kalkhoran and Sforza[13] have focused on the intersection of streamwise vortices, of various strengths, with oblique shock waves and their effect on the aerodynamic characteristics of the shock-generating surface.

Several computations have been performed in order to numerically simulate shock-wave/vortex interactions. Solutions of both the Euler[4,7,8] and Navier–Stokes[6,10] equations have been obtained. Typically, the flow was assumed to be either axisymmetric[4,6,10] or two dimensional.[8] Metwally et al.[6] present results for the axisymmetric Navier–Stokes equations, including a two-equation turbulence model, which were employed to calculate the strong interaction between a normal shock wave and a vortex. The vortex velocity profile was prescribed by experimental data. Corpening and Anderson[7] solved the three-dimensional Euler equations for an oblique shock-wave/vortex interaction at Mach numbers of 2.28 and 5.0. A profile was assumed for the vortex velocity distribution, and a rather coarse mesh of finite volume cells was used. The computations of Meadows et al.[8] also employed an assumed vortex velocity profile to simulate a normal shock-wave/vortex interaction by solving the two-dimensional Euler equations. Kandil et al.[10] considered the laminar axisymmetric Navier–Stokes equations in order to study the supersonic flow in a circular duct. This was the same configuration investigated by Delery et al.,[4] who solved the Euler equations. Once again, an assumed vortex velocity profile was utilized.

In all of the cited numerical simulations, no direct comparisons were provided between the computations and any experimental data. The present investigation attempts to numerically reproduce a physical flow situation, without prior assumptions regarding the form of the vortex velocity profile, for which experimental measurements are available in order to assess the ability of the computations to duplicate the flow physics. For this purpose, the experiment of Kalkhoran and Sforza[13] was selected, which considered the flow in a wind tunnel past the combination of a vortex-generating fin and a wing surface producing an oblique shock.

The configuration is depicted schematically in Fig. 1 and consists of air flow at a freestream Mach number of 3.1 and unit Reynolds number of 8.4×10^7/m through a wind tunnel with a cross section that is 254 mm wide and 262 mm high. A streamwise vortex is produced by the vortex-generating fin, which has sharp leading and trailing edges and a sharp tip. The fin is 119 mm long, 76 mm wide, and 8 mm

Presented as Paper 94-2304 at the AIAA 25th Fluid Dynamics Conference, Colorado Springs, CO, June 20–23, 1994; received June 24, 1994; revision received Dec. 15, 1994; accepted for publication Dec. 20, 1994.

*Research Aerospace Engineer, Computational Fluid Dynamics Research Branch, Aeromechanics Division. Associate Fellow AIAA.

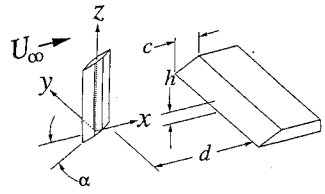

Fig. 1 Vortex generator/wing configuration.

thick. A Cartesian coordinate system was oriented with its vertical (z) axis running through the center of the fin cross section and with its origin at the fin tip (see Fig. 1). The vortex generator was attached to the ceiling of the wind tunnel and rotated about the z axis to angles of attack α, which were taken to be positive when the fin leading edge was located at $y < 0$. In this way, a tip vortex was produced, whose strength could be controlled by varying the angle of attack.

Downstream of the vortex generator, a shock-generating surface was used to produce an oblique shock wave. This surface consisted of a wing that spanned the width of the wind tunnel and had a two-dimensional wedge as its airfoil sectional shape. The wing was 102 mm long and 19 mm thick and had a sharp leading-edge wedge angle of 27.0 deg. The streamwise distance from the leading edge to the upper surface expansion corner was 37.4 mm and has been defined as the reference chord c. In the wind-tunnel model, a series of pressure taps were located along the upper surface between the leading edge and the expansion corner at three spanwise stations in order to collect time-averaged data (see Ref. 13). The leading edge of the wing was situated a distance $d = 157$ mm downstream of the trailing edge of the vortex generator with $\alpha = 0$ deg. The wing leading edge was positioned a distance h below the vertical location of the tip of the vortex generator. This height could be varied in order to bring the core of the vortex closer to or farther from the wing surface.

Although vortex breakdown was not detected in many of the experimental cases, unsteadiness often occurred. As noted by Corpening and Anderson,[7] vortex breakdown may not occur in oblique shock-wave interactions when the postshock flowfield remains supersonic, unlike the normal-shock situation where subsonic flow occurs. It was observed, however, that when the vortex core impinged near to the wing leading edge, the flowfield was unable to support an attached shock wave.[12,13] Locally then, a detached shock wave formed ahead of the wing surface. Near its most upstream extent, this "vortex distortion shock" became normal to the oncoming stream, with a resultant subsonic flow region immediately behind it. This subsonic region allowed for the upstream propagation of disturbances created by the vortex distortion which moved the shock wave upstream of the wing leading edge and displaced it from its original attached position. The detachment phenomenon appeared to be an unsteady process that occurred predominantly when the vertical position of the wing h was such that the vortex core impacted the wing leading edge.

The objective of the present investigation is to duplicate the experimentally observed oblique shock-wave/vortex interactions by solution of the time-dependent three-dimensional compressible Euler and mass-averaged Navier–Stokes equations. In viscous calculations, effects of turbulence are accounted for by a simple algebraic eddy viscosity model. The numerical procedure is summarized, and grid studies are provided in order to assess resolution and accuracy requirements of the solutions. Numerical results are computed for vortices of varying strengths, corresponding to angles of attack of the vortex generator of $\alpha = 5.0, 7.5$, and 10.0 deg. At each angle of attack, cases are calculated for several values of the vertical wing location h. Solutions are presented for the Euler and both the complete and thin-layer Navier–Stokes equations. Characteristics of the numerically generated flowfields are examined, and the computations are compared to experimental data in terms of static pressure distributions on the wing surface.

Governing Equations

The governing equations were taken to be the unsteady compressible three-dimensional Euler and mass-averaged Navier–Stokes equations. The Sutherland law for the molecular viscosity coefficient and the perfect gas relationship were employed, and Stokes' hypothesis for the bulk viscosity coefficient was invoked. Effects of turbulence were accounted for by specifying a turbulent Prandtl number of 0.90 and by incorporating a simple description of the eddy viscosity coefficient. For this purpose the two-layer algebraic model of Baldwin and Lomax[14] was utilized.

Numerical Procedure

Solutions to the governing equations were obtained numerically using the implicit approximately factored finite difference algorithm of Beam and Warming,[15] which has evolved as an efficient tool for obtaining solutions to a wide variety of complex fluid flow problems. First-order Euler implicit time differencing was employed along with second-order accurate central-difference approximations for all spatial derivatives. Common forms of both implicit and explicit nonlinear dissipation[16] were utilized to augment stability, with the pressure gradient parameter given according to Swanson and Turkel.[17] Usual values of user defined damping coefficients were assigned, and for viscous calculations the dissipation was scaled by the square of the local velocity magnitude so that it essentially vanished in regions adjacent to solid surfaces. Efficiency was further increased by solving the implicit portion of the factorized equations in diagonalized form.[18]

The aforementioned features of the numerical algorithm are embodied in an existing fully vectorized time-accurate three-dimensional computer code. This code has proven to be reliable for a number of both steady and unsteady fluid flow problems, including the simulation of supersonic flows with shock waves,[19,20] flows over delta wings with leading-edge vortices,[21–24] and vortex breakdown.[23,24]

The numerical flowfield for the vortex generator/wing combination was partitioned into two distinct computational blocks. These were used to describe the flows separately about the vortex generator and the wing surface, respectively. In addition to standard fine grids for each domain, coarse and medium meshes were also generated for the purpose of resolution studies. Mesh parameters for the computational grids appear in Table 1 for the representative case $\alpha = 10.0$ deg and $h/c = -0.100$. These parameters for other values of α and h are essentially the same.

A complete description of the calculations, including the exact geometry of the configuration, the form of the governing equations, generation of the meshes, specification of the boundary conditions, and details of the time-marching procedure, may be found in Ref. 25.

Results

Although the numerical flowfields were evolved in a time-accurate manner, no unsteadiness was observed for any computations of either the vortex generator or the wing surface. Every solution appeared to converge to a steady state. Apart from the grid resolution study, all of the results presented here correspond to calculations performed on the finest computational meshes. At each value of α, solutions to the Euler equations were obtained for values of $h/c = 0.400, 0.067, -0.100$, and -0.267. These choices were dictated by the experimental geometry. For the purpose of comparison, at $\alpha = 10.0$ deg thin-layer Navier–Stokes solutions were also calculated for all values of h/c. In addition, one solution to the full Navier–Stokes equations was obtained for $\alpha = 10.0$ deg and $h/c = -0.100$.

Vortex Generator

The primary function of the vortex generator is to produce a streamwise vortex which is convected downstream into the wing surface flowfield. Because of the high Reynolds number involved and lack of appreciable inviscid/viscous interaction, the vortex generator domain was simulated numerically only by solutions to the Euler equations for $\alpha = 5.0, 7.5$, and 10.0 deg. It previously has been demonstrated[26] that for supersonic flows over delta wings with sharp edges, where the separation point of a primary vortex is fixed at the leading edge, solutions to the Euler equations afford an approximate representation of the proper total pressure loss within the vortex core. This situation is similar to that of the vortex-generating fin, which also has sharp edges.

Table 1 Computational mesh parameters

Flowfield	Mesh designation	Mesh size	$\Delta S_{\xi\min}$	$\Delta S_{\eta\min}$	$\Delta S_{\zeta\min}$	$\overline{y^+}$	$\overline{N^+}$
Vortex generator	Coarse	$116 \times 51 \times 51$	1.36×10^{-3}	1.77×10^{-5}	1.98×10^{-5}		
$\alpha = 10.0$ deg	Medium	$174 \times 77 \times 77$	8.81×10^{-4}	1.56×10^{-5}	1.57×10^{-5}		
	Fine	$231 \times 101 \times 101$	6.77×10^{-4}	8.85×10^{-6}	8.89×10^{-6}		
Wing, inviscid	Coarse	$121 \times 51 \times 52$	3.16×10^{-4}	1.77×10^{-5}	1.69×10^{-4}		
$\alpha = 10.0$ deg	Medium	$181 \times 77 \times 78$	1.98×10^{-4}	1.56×10^{-5}	1.15×10^{-4}		
$h/c = -0.100$	Fine	$241 \times 101 \times 102$	1.50×10^{-4}	8.85×10^{-6}	8.24×10^{-5}		
Wing, viscous	Coarse	$121 \times 51 \times 52$	4.11×10^{-6}	1.77×10^{-5}	3.45×10^{-6}	2.22	3
$\alpha = 10.0$ deg	Medium	$181 \times 77 \times 78$	3.13×10^{-6}	1.56×10^{-5}	2.27×10^{-6}	1.45	4
$h/c = -0.100$	Fine	$241 \times 101 \times 102$	2.02×10^{-6}	8.85×10^{-6}	1.53×10^{-6}	1.14	5

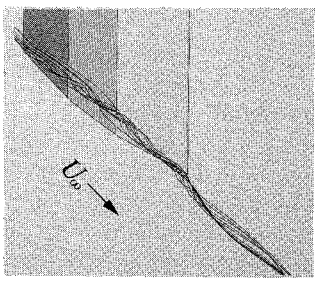

Fig. 2 Particle paths of Euler solution at tip of vortex generator for $\alpha = 10.0$ deg.

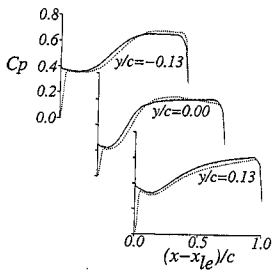

Fig. 4 Wing surface static pressure distributions of solutions for α 10.0 deg and $h/c = -0.100$: —, Navier–Stokes; - - -, thin layer; · · ·, Euler.

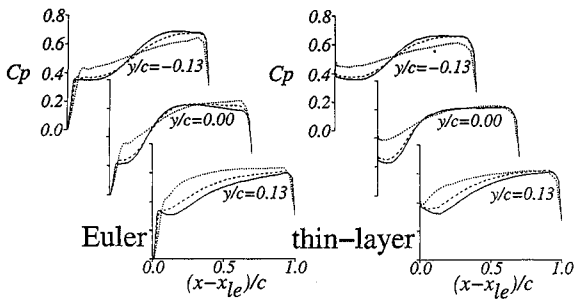

Fig. 3 Effect of grid resolution on wing surface static pressure distributions of Euler and thin-layer solutions for $\alpha = 10.0$ deg and $h/c = -0.100$: —, fine grid; - - -, medium grid; · · ·, coarse grid.

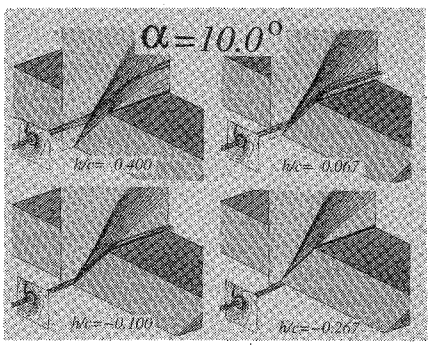

Fig. 5 Total pressure contours, Mach number contours, and particle paths of thin-layer solutions.

Shown in Fig. 2 are particle paths that form at the vertical tip of the fin for $\alpha = 10.0$ deg. As noted, formation of the tip vortex is similar to that of the primary vortex formed at the leading edge of a delta wing at angle of attack in supersonic flow, which has been the subject of a number of investigations.[19,26] Because the helical path lines are produced by the flow expanding around the end of the fin, the core of the vortex lies above the vertical plane of the generator tip.

Grid Resolution

Grid resolution studies were performed for solutions to both the Euler and the thin-layer Navier–Stokes equations. The case $\alpha = 10.0$ deg and $h/c = -0.100$ was selected in this investigation for two reasons. First, it produced the strongest vortex, and second it was found experimentally that in this case the vortex core impacted very nearly on the wing leading edge. It should be noted that for $h/c < 0$, the vertical location of the wing leading edge is actually above that of the vortex generator tip.

Each respective grid of the vortex generator flowfield (coarse, medium, fine) was used in conjunction with its corresponding counterpart for the wing surface domain in order to obtain numerical solutions for the combined configuration. Results of these computations are presented in terms of the wing surface static pressure distributions at the three spanwise stations for which experimental data measurements were taken ($y/c = -0.13, 0.00, 0.13$). Figure 3 indicates that solutions on the medium and fine grids appear to be acceptable for both the Euler and thin-layer Navier–Stokes equations.

Details of the Flowfield

Static pressure distributions on the wing surface for $\alpha = 10.0$ deg and $h/c = -0.100$ are compared for Euler, thin-layer, and full Navier–Stokes solutions in Fig. 4. Only a slight difference is observed between the Euler and thin-layer solutions. Most of this difference is attributed to greater streamwise resolution near the wing leading edge in the thin-layer result. In retrospect, the Euler computational mesh could have been made finer in this region. It is seen in the figure that the thin-layer and full Navier–Stokes solutions are virtually indistinguishable from each other.

Features of the wing surface flowfield corresponding to solutions of the thin-layer Navier–Stokes equations for $\alpha = 10.0$ deg and all values of h/c are displayed in Fig. 5. Contours of constant total pressure are shown near the upstream wing domain boundary and indicate the presence of the tip vortex. The wake of the upstream vertical fin can also be seen to the left of the vortex. Particle paths forming the vortex core pass through the plane of total pressure contours and proceed downstream. For each value of h/c, individual particle paths pass through identical physical locations in the plane of total pressure contours. Above the wing surface, contours of constant Mach number are displayed at a spanwise position that coincides approximately with that of the vortex core and evidence the oblique shock wave which forms at the leading edge. Note that the vertical location of the vortex upstream is constant but that the height of the wing surface increases as h/c decreases. The flow approaching the wing surface has a higher Mach number in the lower portion of the plane of the Mach number contours due to expansion

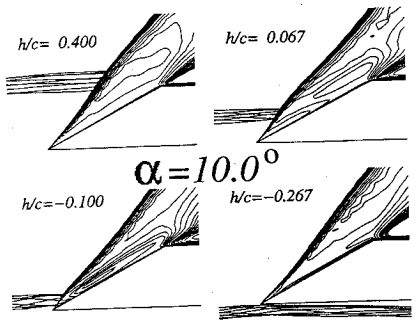

Fig. 6 Mach number contours and particle paths of thin-layer solutions.

in the vertical direction about the vortex generator tip that produces the tip vortex.

It is visible in the figure that for $h/c = 0.400$, the vortex intersects the shock wave well above the wing surface. Some distortion of the shock wave is apparent. For $h/c = 0.067$, the vortex lies nearer to the wing surface, and when $h/c = -0.100$ the vortex almost impacts the wing leading edge directly. In the case of $h/c = -0.267$, which was the highest position of the wing considered experimentally, the vortex actually passes beneath the wing surface. The presence of the vortex moderates the expansion over the aft corner, which is strongest for $h/c = -0.267$ when the vortex is absent. It should be pointed out that no vortex breakdown was ever observed numerically.

The particle paths and Mach number contours appearing in Fig. 5, but viewed in a constant y plane, are shown in Fig. 6. For clarity, the particle paths are not delineated after they intersect with the oblique shock wave. The viewing point for each value of h/c is at a fixed position with respect to the wing surface. When $h/c = 0.400$, a steepening shock-wave angle is seen to form locally where the vortex crosses the oblique shock surface. A more pronounced "bulge" in the shape of the shock geometry can be seen for $h/c = 0.067$. As mentioned earlier, for $h/c = -0.100$ the vortex impinges close to but above the wing leading edge, and for $h/c = -0.267$, the vortex can be seen to pass under the wing surface. In this case the vortex, which travels along a slightly upward trajectory from the vortex-generating fin, is deflected downward as it reaches the wing lower surface. This downward deflection appears to be an inviscid wall interference effect, as it was identical for both the Euler and thin-layer solutions.

It should be remarked that for all values of h/c, distortion of the shock geometry was partially attributable to the nonuniform condition of the upstream flow produced by expansion about the vortex generator tip, as well as to the vortex itself. Although this distortion was appreciable in some cases, it never occurred to such an extent that the shock wave became normal locally, and thus the postshock state was always supersonic.

The "convex-concave" shape of the shock produced by vortex interaction is identical to that observed by Corpening and Anderson.[7] They properly attributed the cause of this behavior to the nonuniform velocity distribution across the vortex core. Because of swirl, velocity components on opposite sides of the core, for example, will intersect the shock wave at unequal angles. In addition, the defect in the streamwise velocity component of the core promotes the indicated bulge. Unlike the solutions of Corpening and Anderson, however, no lateral deflection of the vortex or crossplane flow reversal was observed in the present case.

Limiting streamline patterns on the wing upper surface for $h/c = -0.100$ are presented in Fig. 7. Looking downstream, the vortex rotates in a counterclockwise direction. Thus the surface pattern, which shows flow from left to right near the spanwise region of the vortex, clearly indicates that the vortex lies above the wing. As the vortex particles move downstream from the leading edge, they come in close proximity to the slanted wing upper surface, which tends to annihilate the vortical structure. This occurs upstream of the expansion corner where the surface streamlines are seen to become straight, and remain so over the downstream portion of the wing surface. No evidence of flow separation is apparent.

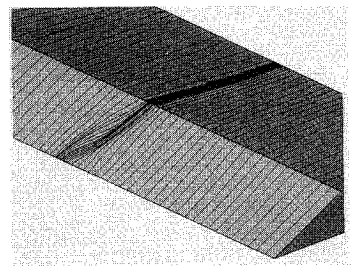

Fig. 7 Limiting streamline patterns on wing surface of thin-layer solution for $\alpha = 10.0$ deg and $h/c = -0.100$.

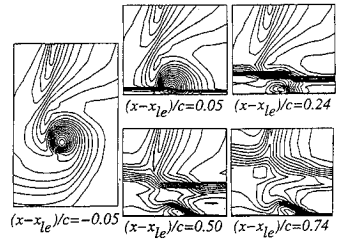

Fig. 8 Total pressure contours of thin-layer solution for $\alpha = 10.0$ deg and $h/c = -0.100$.

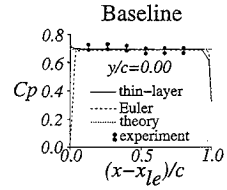

Fig. 9 Wing surface static pressure distributions of thin-layer, Euler, and theoretical solutions and experimental data for baseline case.

Interaction of the vortex with the oblique shock wave is shown in Fig. 8 in terms of total pressure contours in planes at constant streamwise locations as seen looking downstream. At $(x - x_{le})/c = -0.05$ the vortex is shown immediately upstream of the wing leading edge. In the remaining views, the lower boundary of each frame coincides with the wing upper surface. Just downstream of the leading edge $[(x - x_{le})/c = 0.05]$, the vortex core and the shock intersect. When $(x - x_{le})/c = 0.24$, the vortex lies beneath the shock and appears to have been compressed between the shock and wing surface. It has diminished in size and become flat and oval. Farther downstream $[(x - x_{le})/c = 0.50]$, the vortex has lost much of its strength. The numerical shock is smeared due to coarseness of the grid. Finally, at $(x - x_{le})/c = 0.74$ the vortex is devoid of much of its previous structure. This is consistent with the surface streamline patterns of Fig. 7. Although some of the deterioration of the vortex is due to viscous dissipation, this general behavior was essentially the same in the inviscid computation. As is customary with central-difference algorithms, both the Euler and Navier–Stokes computations required explicitly added numerical damping in order to maintain stability, which may have contributed to deterioration of the vortex.

Comparison with Experiment

Comparisons of computational results with experimentally measured wing surface static pressure distributions appear in Figs. 9–12. All experimental[13] data have been time averaged. The double symbols used for the measured data points in these figures represent the experimental uncertainty in pressure coefficient, which was ±0.018. Because of the steady state attained by the computations, averaging was not required for the numerical solutions. Figure 9 indicates pressure distributions from both Euler and thin-layer solutions for the flow over the wing surface when the vortex generator is not present. This situation was referred to experimentally as the baseline case. Also seen in the figure is the two-dimensional inviscid

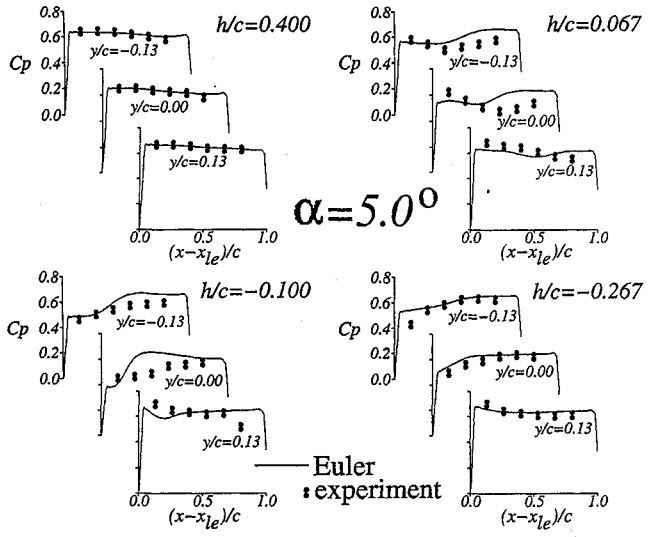

Fig. 10 Wing surface static pressure distributions of Euler solutions and experimental data.

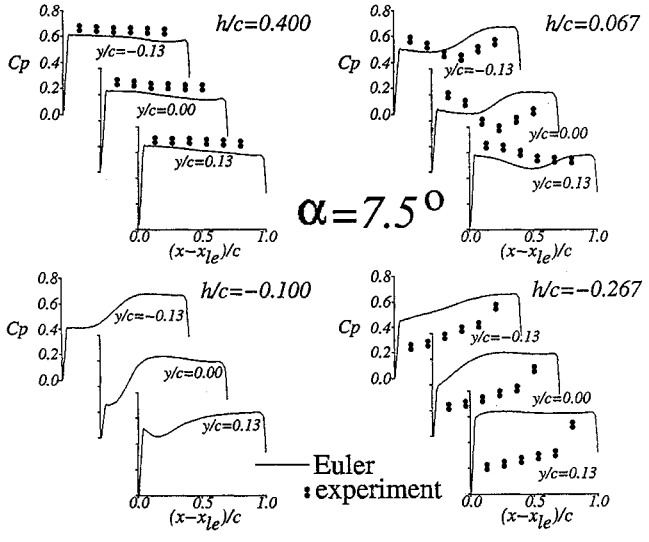

Fig. 11 Wing surface static pressure distributions of Euler solutions and experimental data.

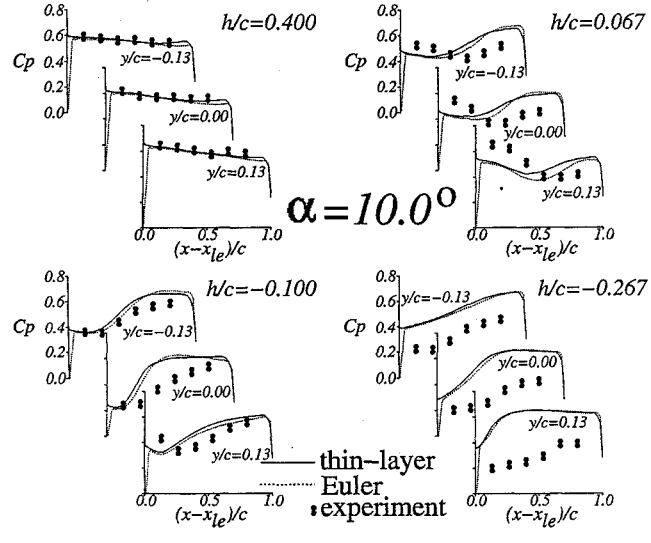

Fig. 12 Wing surface static pressure distributions of thin-layer and Euler solutions and experimental data.

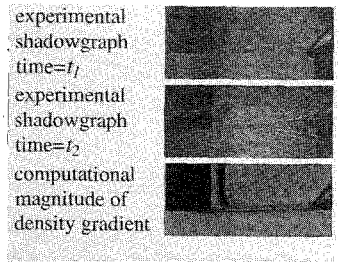

Fig. 13 Flowfield visualization of thin-layer solution and experimental data for $\alpha = 10.0$ deg and $h/c = -0.100$.

theoretical pressure level, which compares well with both computed results and with experimental data.

Numerical solutions to the Euler equations for $\alpha = 5.0$ deg are presented in Fig. 10. Good agreement between the computation and experiment is evident for $h/c = 0.400$, which represents the weakest interaction. This not withstanding, a decrease in the pressure level from the baseline case due to the presence of the vortex is indicated. When $h/c = 0.067$ there is some disparity between the calculation and measurements, particularly at midspan ($y/c = 0.00$). This is also true for $h/c = -0.100$, which shows some additional differences at $y/c = 0.13$. A large degradation in the leading-edge pressure due to the vortex is observed. Reasonable agreement between the numerical solution and experiment exists for $h/c = -0.267$.

A similar comparison for $\alpha = 7.5$ deg is provided in Fig. 11. Here, the disparity between the numerical solutions and the experimental data is greater. Even when $h/c = 0.400$, the computed pressure level is below that of the experiment. For $h/c = 0.067$, the Euler solution predicts a lower leading-edge pressure and higher downstream level than the experiment. Although no measurements were taken at $h/c = -0.100$, the computational result is provided for completeness. The extremely low-experimental-pressure values for $h/c = -0.267$ are probably due to the occurrence of vortex breakdown, which was not seen numerically.

Results for $\alpha = 10.0$ deg appear in Fig. 12. In addition to the Euler calculations, thin-layer Navier–Stokes solutions are also displayed. Acceptable agreement between the computations and experiment is apparent for $h/c = 0.400$. Similar to the behavior at $\alpha = 7.5$ deg, when $h/c = 0.067$ the computed pressures are lower than the experimental levels near the leading edge and higher downstream. Generally good agreement occurs for $h/c = -0.100$ except at $y/c = 0.00$. Once again, the disparity is greatest for $h/c = -0.267$ where the experiment would seem to predict vortex breakdown based on the measured surface pressures. For all values of h/c, only slight variations between the Euler and thin-layer solutions are evident.

Upon comparing Figs. 10–12 for any specific vertical height, the numerical solutions exhibit a consistent trend of decreasing surface pressure for increasing angle of attack. It would seem logical that this should occur as the strength of the vortex increases, thereby reducing the core pressure. Typically, this is also true for the experiment, except when $h/c = 0.400$ where levels are slighter higher for $\alpha = 7.5$ deg than they are for $\alpha = 5.0$ deg.

A visual comparison of the shock-wave/vortex flowfield between the experiment and the thin-layer solution for $\alpha = 10.0$ deg and $h/c = -0.100$ is provided in Fig. 13. The experimental sequential spark shadowgraphs from Ref. 13 were generated at two distinct values of time during the unsteady investigation. At time t_1 no breakdown is indicated, whereas at a later time t_2, a large portion of the vortex has experienced breakdown, considerably altering the flowfield structure. Computational results are presented as contours of magnitude of the density gradient. The dark area seen downstream of and parallel to the fin trailing edge is a portion of the expansion region which forms outboard of the lateral suction surface of the fin as it is viewed in the plane of the contours. The computational result is observed to be quite similar to the experiment at t_1 when breakdown is absent.

Flow conditions of the current calculations are similar to those of Corpening and Anderson[7] who considered freestream Mach numbers of 2.28 and 5.0 for oblique shock waves corresponding to

wedge angles of 20.0 and 32.8 deg, respectively. They employed a Burgers' vortex to numerically simulate oblique shock-wave/vortex interactions and also found no evidence of vortex breakdown for solutions to the three-dimensional Euler equations.

Summary and Conclusions

High Reynolds number supersonic flowfields were generated numerically in order to simulate the flow past a combined vortex-generating fin and wing surface configuration enclosed within a wind tunnel. A comprehensive study was performed for varying strengths of the tip vortex, which was determined by adjusting the vortex generator angle of attack. At each angle, several vertical positions of the wing surface were considered. Solutions were obtained to the Euler, thin-layer, and full Navier–Stokes equations.

Grid studies indicated that resolution on the finest grids was sufficient to describe features of the flow for the present application. Adequate numerical accuracy for engineering purposes, however, could be achieved by employing approximately only one-half the number of fine mesh points for either the vortex generator or wing surface computational domain. Comparison between the Euler, thin-layer, and full Navier–Stokes solutions showed that the simulated phenomena were predominantly inviscid. Thus, meaningful wing surface static pressure distributions resulted from Euler calculations. Details of the numerical flowfield were elucidated and supported the inviscid nature of the shock/vortex interaction.

Computed results were compared to time-averaged experimental data in terms of wing surface static pressure distributions. Although unsteadiness was observed in the experiment, all numerical solutions attained a steady state. Reasonable agreement between the calculations and experimental data was found for $\alpha = 5.0$ deg, corresponding to the weakest vortex. As the vortex strength increased, the agreement was less favorable. Shadowgraphs indicated that over a portion of the unsteady cycle during experimental data collection, in some instances vortex breakdown occurred. Thus, the time-averaged pressures included periods characterized by transient breakdown. Because the numerical solutions were steady and never evidenced any vortex breakdown, the calculations differed from the experiment in these cases.

One deficiency of the present investigation is a lack of any quantitative validation that the simulated vortex approaching the wing surface matches that generated experimentally in size and strength. Moreover, vortex breakdown may be quite sensitive to these parameters. Although grid studies were performed, it was difficult to adequately resolve all critical flow regions, which included those adjacent to solid walls, the entire streamwise vortical structure, and the three-dimensional shock surface. This task could perhaps be facilitated by employing embedded and/or solution adaptive meshes. Also, use of a flux-difference split or upwind-based numerical algorithm may produce higher acuity in shock capturing by avoiding the necessity of artificial dissipation. Finally, the effect of viscosity in vortex generation and the effect of turbulence upon the vortex core, which have been neglected in these computations, may also have an impact on vortex breakdown.

Acknowledgments

Computational resources for the work presented here were provided through the auspices of the Department of Defense High Performance Computing Center at the U.S. Army Corps of Engineers Waterways Experiment Station, Vicksburg, MS. The author is grateful to I. M. Kalkhoran and F. Y. Wang for supplying details of the experiment.

References

[1]George, A. R., "Helicopter Noise: State-of-the-Art," *Journal of Aircraft*, Vol. 15, No. 11, 1978, pp. 707–715.

[2]Pao, S. P., and Seiner, J. M., "Shock-Associated Noise in Supersonic Jets," *AIAA Journal*, Vol. 21, No. 5, 1983, pp. 687–693.

[3]Zatoloka, V. V., Ivanyushkin, A. K., and Nikolayev, A. V., "Interference of Vortices with Shocks in Airscoops: Dissipation of Vortices," *Fluid Mechanics, Soviet Research*, Vol. 7, No. 4, 1978, pp. 153–158.

[4]Delery, J., Horowitz, E., Leuchter, O., and Solignac, J. L., "Fundamental Studies of Vortex Flows," *La Recherche Aerospatiale*, No. 2, 1984, pp. 1–24.

[5]Liu, C. H., "Admissible Upstream Conditions for Slender Compressible Vortices," AIAA Paper 86-1093, May 1986.

[6]Metwally, O. M., Settles, G. S., and Horstman, C. C., "An Experimental Study of Shock Wave/Vortex Interaction," AIAA Paper 89-0082, Jan. 1989.

[7]Corpening, G., and Anderson, J. D., "Numerical Solutions to Three-Dimensional Shock Wave/Vortex Interaction at Hypersonic Speeds," AIAA Paper 89-0674, Jan. 1989.

[8]Meadows, K. R., Kumar, A., and Hussaini, M. Y., "Computational Study on the Interaction Between a Vortex and a Shock Wave," *AIAA Journal*, Vol. 29, No. 2, 1991, pp. 174–179.

[9]Kalkhoran, I. M., Sforza, P. M., and Wang, F. Y., "Experimental Study of Shock-Vortex Interaction in a Mach 3 Stream," AIAA Paper 91-3270, Sept. 1991.

[10]Kandil, O. A., Kandil, H. A., and Liu, C. H., "Supersonic Quasi-Axisymmetric Vortex Breakdown," AIAA Paper 91-3311, Sept. 1991.

[11]Cattafesta, L. N., and Settles, G. S., "Experiments on Shock/Vortex Interaction," AIAA Paper 92-0315, Jan. 1992.

[12]Kalkhoran, I. M., "Vortex Distortion During Vortex-Surface Interaction in a Mach 3 Stream," *AIAA Journal*, Vol. 32, No. 1, 1994, pp. 123–129.

[13]Kalkhoran, I. M., and Sforza, P. M., "Airfoil Pressure Measurements During Oblique Shock Wave-Vortex Interaction in a Mach 3 Stream," *AIAA Journal*, Vol. 32, No. 4, 1994, pp. 783–788.

[14]Baldwin, B. S., and Lomax, H., "Thin Layer Approximation and Algebraic Model for Separated Turbulent Flows," AIAA Paper 78-257, Jan. 1978.

[15]Beam, R., and Warming, R., "An Implicit Factored Scheme for the Compressible Navier–Stokes Equations," *AIAA Journal*, Vol. 16, No. 4, 1978, pp. 393–402.

[16]Jameson, A., Schmidt, W. and Turkel, E., "Numerical Solutions of the Euler Equations by Finite Volume Methods Using Runge–Kutta Time Stepping Schemes," AIAA Paper 81-1259, June 1981.

[17]Swanson, R. C., and Turkel, E., "On Central-Differencing and Upwind Schemes," *Journal of Computational Physics*, Vol. 101, No. 2, 1992, pp. 292–306.

[18]Pulliam, T. H., and Chaussee, D. S., "A Diagonal Form of an Implicit Approximate-Factorization Algorithm," *Journal of Computational Physics*, Vol. 39, No. 2, 1981, pp. 347–363.

[19]Webster, W. P., and Shang, J. S., "Thin-Layer Full Navier–Stokes Simulations over a Supersonic Delta Wing," *AIAA Journal*, Vol. 29, No. 9, 1991, pp. 1363–1369.

[20]Rizzetta, D. P., "Numerical Simulation of Turbulent Cylinder Juncture Flowfields," AIAA Paper 93-3038, July 1993.

[21]Gordnier, R. E., and Visbal, M. R., "Numerical Simulation of Delta-Wing Roll," AIAA Paper 93-0554, Jan. 1993.

[22]Gordnier, R. E., "Computation of Delta-Wing Roll Maneuvers," AIAA Paper 93-2975, July 1993.

[23]Visbal, M. R., "Structure of Vortex Breakdown on a Pitching Delta Wing," AIAA Paper 93-0434, Jan. 1993.

[24]Visbal, M. R., "Computational Study of Vortex Breakdown on a Pitching Delta Wing," AIAA Paper 93-2974, July 1993.

[25]Rizzetta, D. P., "Numerical Simulation of Oblique Shock-Wave/Vortex Interaction," AIAA Paper 94-2304, June 1994.

[26]Powell, K. G., Murman, E. M., Perez, E. S., and Baron, J. R., "Total Pressure Loss in Vortical Solutions of the Conical Euler Equations," *AIAA Journal*, Vol. 25, No. 3, 1987, pp. 360–368.